

Design of a Phased Array for the Generation of Adaptive Radiation Force Along a Path Surrounding a Breast Lesion for Dynamic Ultrasound Elastography Imaging

Didace Ekeom, Anis Hadj Henni, and Guy Cloutier

Abstract—This work demonstrates, with numerical simulations, the potential of an octagonal probe for the generation of radiation forces in a set of points following a path surrounding a breast lesion in the context of dynamic ultrasound elastography imaging. Because of the in-going wave adaptive focusing strategy, the proposed method is adapted to induce shear wave fronts to interact optimally with complex lesions. Transducer elements were based on 1–3 piezocomposite material. Three-dimensional simulations combining the finite element method and boundary element method with periodic boundary conditions in the elevation direction were used to predict acoustic wave radiation in a targeted region of interest. The coupling factor of the piezocomposite material and the radiated power of the transducer were optimized. The transducer’s electrical impedance was targeted to 50 Ω . The probe was simulated by assembling the designed transducer elements to build an octagonal phased-array with 256 elements on each edge (for a total of 2048 elements). The central frequency is 4.54 MHz; simulated transducer elements are able to deliver enough power and can generate the radiation force with a relatively low level of voltage excitation. Using dynamic transmitter beamforming techniques, the radiation force along a path and resulting acoustic pattern in the breast were simulated assuming a linear isotropic medium. Magnitude and orientation of the acoustic intensity (radiation force) at any point of a generation path could be controlled for the case of an example representing a heterogeneous medium with an embedded soft mechanical inclusion.

I. INTRODUCTION

DEVELOPMENTS in ultrasound (US) elastography initially aimed at studying changes in stiffness properties of biological organs under pathological conditions [1].

Manuscript received October 23, 2012; accepted December 17, 2012. This research was funded by the Collaborative Health Research Program of the Natural Sciences and Engineering Research Council of Canada (grant #365656-09) and of the Canadian Institutes of Health Research (grant #CPG-95288).

D. Ekeom was with the Laboratory of Biorheology and Medical Ultrasonics, University of Montréal Hospital Research Center (CRCHUM), Montréal, QC, Canada, and is now with Microsonics, Saint-Avertin, France.

A. Hadj Henni was with the Laboratory of Biorheology and Medical Ultrasonics, University of Montréal Hospital Research Center (CRCHUM), Montréal, QC, Canada, and is now with Rheolution Inc., Montréal, QC, Canada.

G. Cloutier is with the Laboratory of Biorheology and Medical Ultrasonics, University of Montréal Hospital Research Center (CRCHUM), Montréal, QC, Canada; the Department of Radiology, Radio-Oncology and Nuclear Medicine, University of Montréal, Montréal, QC, Canada; and the Institute of Biomedical Engineering, University of Montréal, Montréal, QC, Canada (e-mail: guy.cloutier@umontreal.ca).

DOI <http://dx.doi.org/10.1109/TUFFC.2013.2596>

With quasi-static compression of an organ (e.g., a breast), a stiffer tissue region will experience less axial strain than a softer one. Consequently, by color mapping displacements in millimeters and/or deformations in percent, contrast images of suspected lesions can be obtained. After two decades of development, most manufacturers are now offering US elastography packages and clinical validations have been conducted [2]–[5]. However, a major limitation of this imaging method is its high interobserver variability [4], [6]. Improvements may be to compute axial-shear strain elastograms [7], and to use more robust displacement or deformation algorithms. Nevertheless, compression elastography does not give quantitative assessment of tissue stiffness (i.e., Young’s elastic modulus), and artifacts are induced by unknown boundary conditions.

Contrary to quasi-static methods, dynamic elastography was introduced [8]–[10] to map the viscoelasticity of living tissues by studying traveling shear wave properties in the probed medium. The tracking of shear waves with Doppler-based or radio-frequency (RF)-based methods allows local determination of velocity V_s and attenuation α_s in a tissue. Theoretically, viscoelasticity maps can be obtained from measured V_s and α_s by assuming appropriate rheological models of probed tissues. A simpler implementation allows quantitative elasticity maps if one assumes linear, homogeneous, isotropic, incompressible, and non-viscous materials (Hooke’s law gives $G_s \approx 3\rho V_s^2$, where G_s is the shear elasticity modulus and ρ is the tissue density, which is assumed constant). A commercial version of this implementation [11] was introduced for imaging and quantifying the shear elasticity modulus of breast lesions. The proposed technique creates localized quasi-plane shear waves of high amplitude by moving the ultrasonic foci points faster than the shear wave speed at different depths on a straight line. Resulting shear waves interfere constructively along a Mach cone, creating quasi-plane shear wave fronts propagating in opposite directions. According to recent clinical reports [12]–[14], the technique seems reproducible and improves specificity compared with B-mode US alone.

Currently, shear wave elastography implementation is mainly done with a unique shear wave directivity pattern or a quasi-spherical pattern in the case of point vibrations, as summarized next. Quasi-plane shear waves typically perpendicular to the transmitted beam are used for the supersonic imaging method [15], whereas the crawling

wave sonoelastography approach relies on the transmission of two phase-shifted vibrations moving in opposite directions to generate a low-frequency shear wave front [16]. For the ultrasound-stimulated vibro-acoustography method, a confocal transducer transmits beating waves at a focal point [17]. In the case of the acoustic radiation force impulse imaging approach, local vibrations are induced by successively transmitting a high-energy pulse at several focal points [18]. The newly developed shear-wave-induced resonance elastography (SWIRE) method uses horizontal [19] or torsional [20] polarized shear waves. Variants of these different methods also proposed limited shear wave directivity patterns [21]–[23].

The objective of the current study was thus to design a strategy to polarize shear waves in any directions for developments with a goal of providing a new screening method for breast cancer based on shear wave viscoelasticity imaging. In our previous work with SWIRE [20], we proved the efficacy of torsional waves to produce *in vivo* mechanical resonance of a fibroadenoma. However in that study, an external source of vibration was applied at the surface of the breast to produce the torsional wavefront, which is not efficient because of the attenuation of shear waves by breast tissues. The current study demonstrates that an octagonal array, with an appropriate focusing strategy, can produce inward propagating shear waves with torsional wavefronts for *in vivo* applications. A second challenge for inducing torsional shear waves or any types of polarized shear wave fronts is to produce enough energy to generate *in situ* radiation pressure. Our study also demonstrates that this is possible by optimizing material and electronic designs of the proposed octagonal array probe. Note that the current design with 2048 elements was inspired by developments made in the field of breast US computed tomography (CT), for which reflectivity, speed of sound, and attenuation are typically mapped [24]–[26]. To our knowledge, none of these designs considered *in situ* radiation pressure generation.

In detail, the current study shows numerically the feasibility of a piezocomposite US probe that can generate radiation forces in a set of foci points following an arbitrary path (closed or open) around a region of interest (ROI; typically, a tumor). With such an approach, we intend to generate a shear wave front that fits the tumor contour after the propagation of low-frequency in-going shear waves over a couple of wavelengths to induce tissue displacements. To achieve this specification, a high-sensitivity octagonal phased array with 2048 transducer elements was designed. It can theoretically produce an acoustic spatial-peak pulse-average intensity of 190 W/cm² at several foci points simultaneously and generate US radiation forces respecting the guidelines of the U.S. Food and Drug Administration (FDA) [27]. The center frequency of the transducer was set at 4.54 MHz. The transducer's electrical impedance without cable at its resonance frequency was targeted to 50 Ω to match the electrical impedance of standard electrical termination. During the conceptual phase, the voltage excitation was imposed as

low as possible to theoretically limit overheating of transducer elements.

II. TRANSDUCER DESIGN AND SIMULATION

A. Design and Optimization of Piezocomposite Material

The 1–3 piezocomposite was used as active material because it has a high thickness mode coupling factor and because its dielectric constant and acoustic impedance can be tailored. The mechanical impedance was selected to optimize the transmission of acoustic power into the tissue. Several piezoelectric ceramic and polymer materials were envisaged to achieve the targeted application. With regard to its high electromechanical coupling factor and its high dielectric constant, PZT-5H (MTC ElectroCeramics, Thornhill, UK) [28] was selected as the ceramic phase. For the polymer phase we selected Dow epoxy resin loaded with alumina (Dow Chemical Co., Varennes, CQ, Canada), which has a relatively high shear wave velocity [29]. This selection was done to reduce parasitic modes resulting from lateral waves. PZT-5H and Dow material data are given in Table I.

The shape was optimized by considering the piezocomposite texture that has been used for phased-array transducers. The piezocomposite thickness h was fixed to 330 μm , and the polymer width and depth were selected as 250 and 115 μm , respectively. The kerf width separating two neighboring transducer elements was 50 μm . The 1–3 piezocomposite was made of two ceramic pillars with square cross-sections of width L_c . This parameter L_c was a variable to optimize in our simulations (i.e., to optimize according to the volume fraction of PZT-5H).

TABLE I. SIMULATED PIEZOCOMPOSITE PHASE MATERIAL DATA.

Parameter	PZT-5H	Dow
ρ (kg/m ³)	7500	1760
C_{11}^E (GPa)	126	17.8
C_{12}^E (GPa)	79.5	8.6
C_{13}^E (GPa)	84.1	8.6
C_{33}^E (GPa)	117	17.8
C_{44}^E (GPa)	23	8.6
C_{66}^E (GPa)	23.2	4.6
Q_m	195	30
e_{15}	17	0
e_{31}	−6.6	0
e_{33}	23.3	0
k_{33}	0.752	0
k_t	0.505	0
$\varepsilon_{11}^S/\varepsilon_0$	1700	3.9
$\varepsilon_{33}^S/\varepsilon_0$	1470	3.9
$tg \delta_e$	0.01538	0.01333

Parameters: ρ is the density, C_{ij}^E is the elastic stiffness, Q_m is the mechanical quality factor, e_{ij} is the piezoelectric constant, k_{33} is the longitudinal coupling factor, k_t is the thickness coupling factor, $\varepsilon_{ij}^S/\varepsilon_0$ is the relative dielectric constant, and $tg \delta_e$ is the dielectric dissipation factor.

Most values of selected parameters were taken from [28] and [29]; others were estimated.

Other optimization quantities were the thickness-mode coupling factor k_t , the dielectric constant $\varepsilon_{ij}^S/\varepsilon_0$, and the mechanical impedance z_m . Finite element method (FEM; version 12.0, Ansys, Canonsburg, PA) undamped resonance and antiresonance modal analyses were performed for different values of the ceramic phase width (L_c). Only one cell of the piezocomposite material was meshed (Fig. 1). To take into account potential lateral waves propagating in the piezocomposite plate, periodic boundary conditions were applied with Floquet parameters $\gamma_x = \gamma_y = 0$. The electrical resonance frequency F_r and antiresonance frequency F_a were directly extracted from the FEM modal analysis. The thickness-mode coupling factor k_t and mechanical impedance z_m of the piezocomposite plate were then evaluated, respectively, with

$$k_t^2 = \frac{\pi F_r}{2 F_a} \tan\left(\frac{\pi F_r}{2 F_a}\right) \quad (1)$$

$$z_m = 2\rho h F_a, \quad (2)$$

where ρ is the density of the piezocomposite material. FEM electrostatic analyses were also performed for different values of the ceramic phase width L_c . The static capacitance (C_0) was extracted and the dielectric constant of the piezocomposite material was computed with

$$\frac{\varepsilon_{33}^S}{\varepsilon_0} = \frac{C_0 h}{\varepsilon_0 S}, \quad (3)$$

where S is the surface of the active area ($115 \times 250 \mu\text{m}$) and ε_0 is the free-space permittivity. The optimal piezocomposite material could be obtained by adjusting the volume fraction of the ceramic phase. Decreasing the volume fraction decreases the mechanical impedance but causes the deterioration of the coupling factor, and of the dielectric constant, and allows propagation of lateral waves. A trade-off had thus to be made between the low mechanical impedance and high coupling factor and dielectric constant.

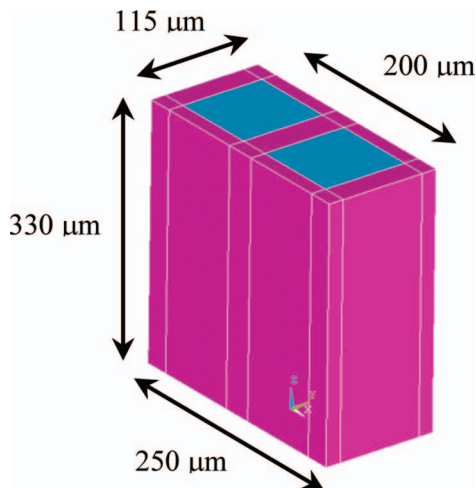
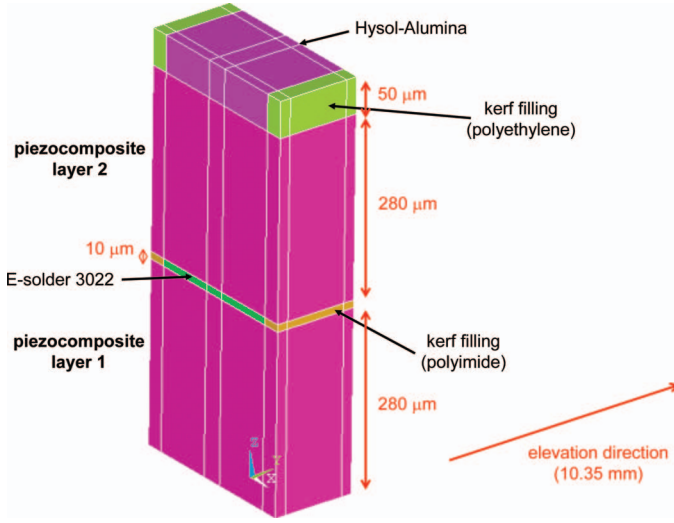


Fig. 1. 1-3 piezocomposite texture of the transducer subelement. 

B. Design and Simulation of the Transducer

The piezocomposite structure designed as described in the previous section was used as the active material of the transducer. To amplify the radiating acoustic power for a given voltage, two piezocomposite layers with opposite polarization were assembled and the transducer was air-backed. This choice has the advantage of limiting the driving voltage, and hence avoiding overheating of the transducer. It also helped to match the electrical impedance to the targeted value of 50Ω . Another advantage of the new transducer design that can produce radiation power at a low voltage is to avoid redesigning the front-end and power supply of the US scanner for future experimental validation. Because the mechanical impedance of the piezocomposite layer is one magnitude higher than that of biological tissues, a matching layer with intermediate mechanical impedance was needed. We selected a 0-3 composite of Hysol (Henkel Corp., Bay Point, CA) and alumina with 20% volume fraction of aluminum [30] and a matching layer thickness of $50 \mu\text{m}$. Its mechanical impedance and thickness were chosen to optimize the transmission of acoustic power. A continuous matching layer is limiting because of lateral mode propagation that couples energy between neighboring transducer elements. To overcome this problem, the matching layer was diced completely in the elevation direction. The resulting simulated kerf was filled with polyethylene [29]. All electrodes were modeled as being made of $2\text{-}\mu\text{m}$ -thick gold. External electrodes were connected to ground. Internal electrodes were derived and separated by a $10\text{-}\mu\text{m}$ conductive epoxy bonding layer (E-solder 3022 electrically conductive adhesive [31], Von Roll Holding, Wädenswil, Switzerland). This layer was also completely diced to limit propagation of lateral modes. The resulting kerf was filled with polyimide. The transducer elevation dimension was 10.35 mm . Fig. 2 shows the transversal section of a transducer subelement and Table II gives material data considered for the transducer design.

Because transducer elements were air-backed, lateral modes may propagate in the piezocomposite plate. The main concerns for the transducer design were the evaluation of lateral modes in vacuum and in water (frequency positions and electrical impedance amplitude) and the determination of the electroacoustic response. Lateral modes can be generated by periodic structures in the transducer design. FEM simulations with periodic boundary conditions were thus performed in the lateral direction for the Floquet parameter γ_x equal to 0 and 0.5. The electroacoustic response was obtained by combining the FEM approach with the boundary element method (BEM) using a proprietary software plug-in compatible with Ansys (Microsonics, Saint-Avertin, France). A specific rigid-baffle Green's function that takes into account acoustic radiation conditions of the entire transducer in the elevation direction was implemented. Crosstalk between neighboring elements was not taken into consideration.

Fig. 2. Transducer subelement. 

C. Beamforming and Ultrasound Field Simulation

This section deals with US propagation and dynamic beamforming techniques for the proposed transducer design. The goal was to evaluate the US field and the electrical excitation that could generate a given radiation force (magnitude and orientation) at a given focus point inside a ROI typically including a breast tumor.

The fabrication of a circular phased array would need a shaping step, mechanically weakening the device, especially when considering air-backed transducers. However, the fabrication of a polygonal phased array made of several linear arrays does not need any curvature of transducer elements. In this work, we designed an octagonal phased array for hand-held application. Its schematic overview is presented in Fig. 3. The probe was obtained by assembling the previously designed transducer to build the phased array, with 256 elements on each edge. The probed ROI diameter (i.e., an average breast cross section) was supposed to be in the range of 12 to 15 cm. The US coupling medium between the octagonal transducer and the ROI was water. In this section, possible nonlinear acoustic effects on the US field and shear wave propagation within the breast tissue, modeled as water, were neglected. The velocity of compression waves and the density of water used for these simulations are given in Table II. The ROI was located in the far field of the transducer. Each transducer element was supposed to radiate independently in an open half-space rigid baffle. Finally, because the US firing duration to generate the radiation force was typically 100 to 700 cycles, simulations were performed in the frequency domain to increase performance.

Let P in Fig. 3 be the focal point for a given beam orientation within the ROI. The unit vector \vec{u} (or alternatively \mathbf{u}) defines the radiation force orientation (or acoustic axis). The active aperture for a given focal point is chosen with an f-number of 2 so that P_0 is a point located in a transducer array. P_0P has the same orientation as the acoustic axis and P_i describes a given transducer element

TABLE II. SIMULATED MATERIAL DATA OF TRANSDUCER LAYERS AND OF THE COUPLING MEDIUM MIMICKING THE BREAST TISSUE (I.E., WATER FOR THE SIMULATION OF THE US FIELD).

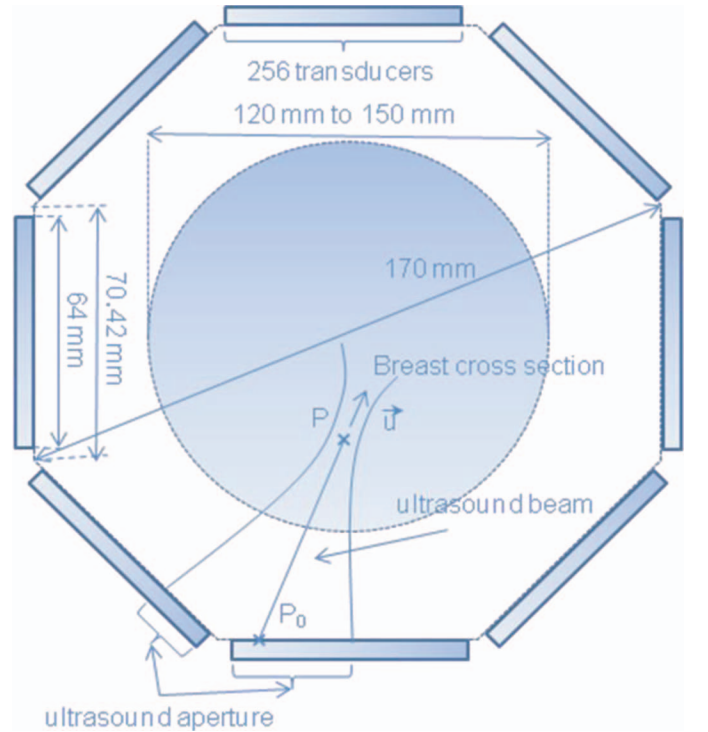
Material	ρ (kg/m ³)	V_c (m/s)	V_s (m/s)	Q_m
E-solder 3022 [31]	3200	1850	840	195
Gold	19320	3194	1186	0
Hysol-alumina [30]	1720	2836	1380	75
Polyethylene [29]	900	1944	527	50
Polyimide	1500	2200	1058	100
Water	1000	1500	—	5000

Parameters: ρ is the density, V_c is the velocity of the compression wave, V_s is the velocity of the shear wave, and Q_m is the mechanical quality factor.

of the US aperture including P_0 . Other parameters relevant to understanding (4) are \mathbf{r} , \mathbf{r}_0 , and \mathbf{r}_i , which are vectors representing the positions of points P , P_0 , and P_i . The electrical potential Φ_i was set to zero for transducer elements located outside the US aperture. Inside the US aperture, for a transducer element located at P_i , the electrical potential Φ_i in the frequency domain was expressed as

$$\Phi_i = \Phi_0 \left(\frac{1}{4} \left| \frac{\mathbf{r}_i - \mathbf{r}_0}{\mathbf{r} - \mathbf{r}_0} \right|^2 + 1 \right) e^{\mathbf{k} \cdot (\mathbf{r}_i - \mathbf{r}) - j|\mathbf{r}_0 - \mathbf{r}|}, \quad (4)$$

where Φ_0 is the electrical potential of the transducer element located at point P_0 ; $|\mathbf{r}_i - \mathbf{r}_0|$ is the distance between transducer elements i and 0 ; $|\mathbf{r} - \mathbf{r}_i|$ for $i = -N_{\text{ap}}/2, \dots, 0, \dots, N_{\text{ap}}/2$, where $N_{\text{ap}} + 1$ is the number of elements in the US aperture, is the distance between the focus point and transducer element i ; \mathbf{k} is the wave number of longitudinal compression waves in the ROI; and j is the pure imaginary

Fig. 3. Schematic cross-sectional view of the octagonal probe around a region of interest (ROI). 

number. The time delay at each element was defined so that all waves arriving at the focal point were in phase. Several apodization functions were tested to limit side lobes in the pressure field. A parabolic apodization was selected with the minimum electrical potential sent to the central transducer element at P_0 , and the maximum potential transmitted at both extremities of the ultrasound aperture.

According to the boundary integral representation, the US pressure field at position x inside the ROI was modeled as

$$P(x) = -\rho\omega^2 U_n \sum_{m=1}^{N_{ap}+1} \Phi_m \int_{\Gamma_m} G(x, x') dS_{x'}, \quad (5)$$

where ρ is the propagating medium density (of water or, equivalently, of the ROI), ω is the angular frequency, U_n is the average normal displacement on Γ_m extracted from the FEM-BEM analysis, Γ_m is the radiating area of the transducer element m , and G is the half-space rigid-baffle acoustic Green's function. The integral of (5) provides a simple but exact three-dimensional representation of the pressure radiating from the active elements of the octagonal phased array, assuming that transducer elements are mounted on a rigid baffle [29]. The Gauss numerical integration procedure was used to calculate this integral accurately. The problem is linearly dependent on Φ_0 . To fit the targeted acoustic intensity at the focal point, Φ_0 could be fixed during the postprocessing.

D. Geometry Considered for Producing a Radiation Force Around a Tumor

Results presented in this study were inspired by the realistic breast lesion geometry presented in Fig. 4. The tumor contour was simplified to an ellipse with a 19.6 mm major axis and a 13.3 mm minor axis. Two realistic elliptic contours with these dimensions but with different locations and orientations are illustrated in Fig. 5. In this study, beamforming simulations to induce radiation pressure were limited to the case of the angulated lesions of Fig. 4 (i.e., top-right lesion of Fig. 5).



Fig. 4. Ultrasound image of a breast with a quasi-elliptic lesion (benign fibroadenoma).

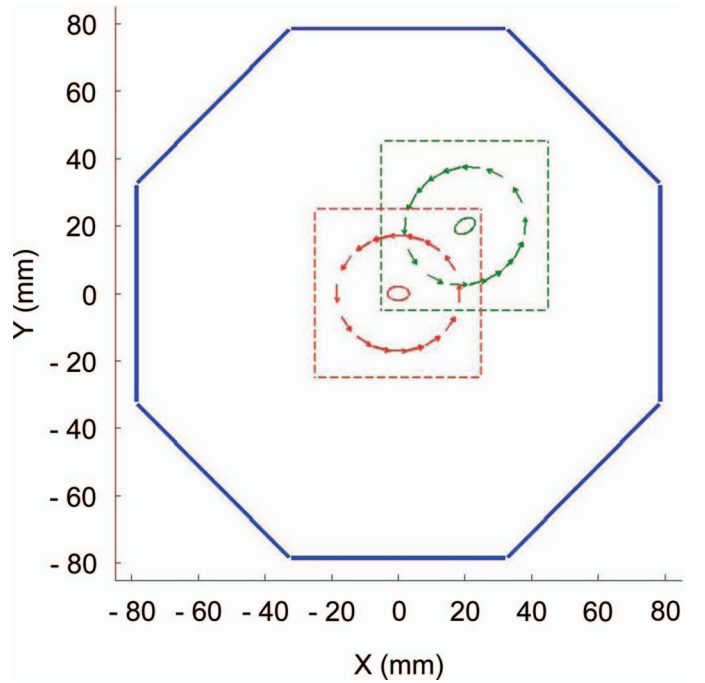


Fig. 5. Focalization paths around two tumors (horizontal ellipse 1 and angulated ellipse 2). Arrows indicate the focalization points of each ultrasound aperture required to produce the radiation pressure path. The translation distance between foci points and the contour of each tumor is adaptable because of the flexibility of the octagonal probe design. Dotted squares simply illustrate regions of interest within a breast. 

As illustrated in Fig. 5, a vector tangent to each point of an enlarged version of the tumor contour was defined to represent the desired radiation force orientation. For each vector, an US aperture oriented in the \vec{u} direction (see Fig. 3) was selected to produce a radiation force aligned with that vector. The translation distance, illustrated in Fig. 5, between the tumor and the radiation force path is flexible and can be modified to favor in-going shear wave concentration and then to increase the shear displacement amplitude in and around the modeled tumor. This distance typically corresponded to some shear wave wavelengths for the targeted intensity of 190 W/cm^2 on the radiation force propagation path.

E. Finite Element Simulation of Low-Frequency Shear Waves

This section presents a two-dimensional simulation of shear waves generated by radiation forces into the probed tissue. The elastodynamic field was obtained by solving the equation of motion in the frequency domain:

$$\rho\omega^2 \mathbf{U} + (\lambda + 2\mu)\nabla(\nabla \cdot \mathbf{U}) - \mu\nabla \times (\nabla \times \mathbf{U}) = \mathbf{F}. \quad (6)$$

In this equation, ρ is the tissue density, ω is the angular frequency, \mathbf{U} is the displacement vector, λ and μ are Lamé viscoelastic coefficients, and \mathbf{F} is the US radiation vector force. To avoid reflections on external boundaries of the meshed domain, a perfectly attenuating matching layer was considered outside of the simulated ROI. The

radiation force \mathbf{F} was assumed to be a 600-Hz harmonic wave defined as a volumic pushing force inducing a motion toward the probed lesion. Its expression can be calculated by [10]

$$\mathbf{F} = \frac{2\alpha_c I \Delta t}{V_c}, \quad (7)$$

where α_c is the US attenuation of compression waves, I is the local acoustical intensity, Δt is the duration of transmitted harmonic waves, and V_c is the velocity of US compression waves in the tissue.

A force vector was defined for each mesh node by considering the simulated radiation force field. First, nonzero force vectors (i.e., amplitude and direction) in the radiation force field were identified and precisely located. Then, the 2-D components (F_x, F_y) of the force vectors were reported to the nodes of the FEM mesh. Because the FEM spatial mesh did not correspond to the mesh of the force field, we implemented a linear interpolation method to match, without discontinuity, force vectors to the FEM nodes. To take into account the presence of mechanical heterogeneities into the propagation medium, different shear moduli G_s (i.e., the value of the second Lamé coefficient μ in (6), which is equivalent to G_s) were attributed to each medium. The first Lamé coefficient λ was fixed to $3 + 0.03i$ GPa. Table III gives simulated values of density and shear modulus G_s for the breast tissue and tumor inclusion.

III. RESULTS

A. Performance of the 1–3 Piezocomposite Material

In these simulations, the ceramic phase length L_c ranged from 37.91 to 96.67 μm . This corresponds to volume fractions of PZT-5H of 0.10 to 0.65. For tested values of L_c (i.e., of volume fractions, because other dimensions were fixed), the thickness-mode coupling factor, dielectric constant, and mechanical impedance were evaluated. Results of Fig. 6 obtained by FEM show the thickness-mode coupling factor versus mechanical impedance of the piezocomposite material. Smith's model [29] (1-D analytical model) is presented for comparison. One can see that Smith's model overestimates the coupling factor because the energy lost in lateral motions was not taken into account. The piezocomposite optimal thickness-mode coupling factor was around 0.56 to 0.58 for a volume fraction of PZT-5H ranging from 0.40 to 0.60. The associated mechanical impedance ranged from 13.71 to 18.55 MRayl and the relative dielectric constant varied from 490 to 673.

B. Performance of the Transducer

The active element of the 1–3 piezocomposite transducer presented in Fig. 2 was formed by two ceramic rods with square cross sections of $85 \times 85 \mu\text{m}$. These dimensions correspond to a ceramic volume fraction of 0.50. Therefore, the associated thickness mode coupling factor

TABLE III. SIMULATED BREAST TISSUE AND TUMOR INCLUSION MATERIAL DATA.

	ρ (kg/m ³)	G_s (Pa)
Breast tissue	1100	70000 + 3500 <i>i</i>
Tumor	1100	40000 + 2000 <i>i</i>

Parameters: ρ is the density and G_s is the viscoelastic shear modulus, the real part corresponds to the storage modulus and the imaginary part to the loss modulus.

was 0.57, the mechanical impedance was 17.38 MRayl and the dielectric constant was $612 \epsilon_0$ (ϵ_0 is the free-space permittivity). The Hysol–alumina 50- μm matching layer on top of the transducer that was necessary to optimize the transfer of acoustical power toward the radiating medium had an impedance of 4.87 MRayl. The transducer was free of lateral modes for operating frequencies between 3 to 6 MHz. Although not quantified, the crosstalk between neighbor transducer elements was likely limited because of the absence of lateral wave propagation. Fig. 7 shows the harmonic impedance of the transducer vibrating in vacuum for two values of the Floquet parameter γ_x (0 and 0.5). One can see that the first lateral mode appears over 6.5 MHz.

The electroacoustical response of the transducer radiating into the tissue (mimicked as water) was calculated and results are displayed in Fig. 8. The resonance and antiresonance frequency peaks were located at 4.51 and 5.58 MHz, respectively. A summary of electroacoustical parameters (without cables) of the simulated transducer is presented in Table IV.

C. Focalization Around a Tumor

As previously mentioned in Section II-D, the shape of a benign fibroadenoma was simplified to an ellipse with a major axis of 19.6 mm and a minor axis of 13.3 mm (major axis angle of 30°). A summary of tested electrical excitation parameters of the octagonal probe that allowed achieving the targeted spatial-peak pulse-average intensity of 190 W/cm² along the elliptic path is provided in Table V. With tested apertures, the lateral beam width was about 1 mm, whereas focal axial dimensions ranged from 8 to 12 mm.

Fig. 9 presents an example of the acoustic intensity field and resulting simulated displacement field achieved with successive focused US beams. The pressure inside the closed path embedding the simulated tumor is about -20 to -30 dB below the pressure along the path. No US beam is crossing the inside domain of the closed path because of the convexity of the radiation pressure pattern. The pressure outside the path is about -10 dB below that of the maximum on the path.

As shown in Fig. 9(a), US beams generated by a set of transducer elements of the octagonal array probe were focused at different positions around the inclined ellipse mimicking the mechanical heterogeneity (i.e., the lesion). For each firing position indicated by an arrow in Fig. 5, a beam was selected to align its focal spot parallel to the

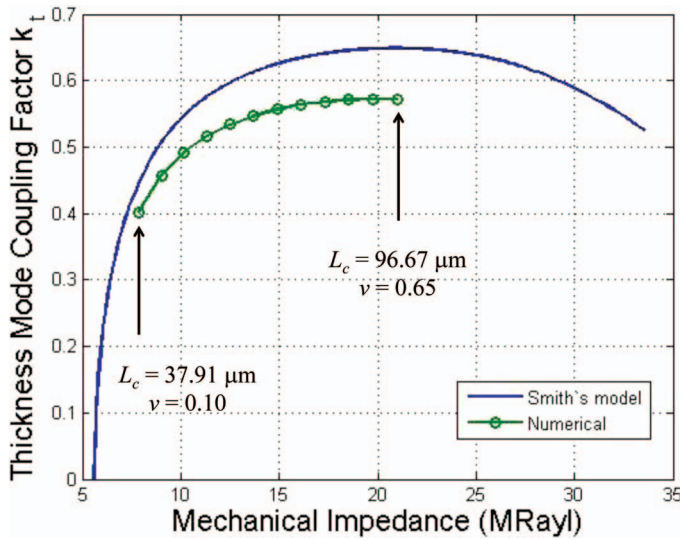


Fig. 6. Thickness-mode coupling factor k_t versus mechanical impedance z_m of the piezocomposite for different PZT-5H volume fractions ν , corresponding to different ceramic phase lengths L_c .

desired radiation force orientation (i.e., parallel to the arrow). Fig. 9(a) displays the intensity of each beam that is mainly concentrated within the focal spot. To generate the desired radiation pressure path, other beams were successively selected to match the other radiation force orientations. By using quasi-simultaneous focusing (i.e., short time delay between successive beams), constructive shear wave patterns as in Fig. 9(b) could be generated. In this example, focal spots of successive moving beams made one turn around the ellipse to create in-going shear waves. In practice, it would be feasible to design a programmable logic multiplexer to sequentially activate the desired elements of the octagonal probe to produce successive moving beams.

For the simulated result of Fig. 9, the elliptic path and inclination angle had to be determined from *a priori*

TABLE IV. ELECTROACOUSTIC PARAMETERS OF THE SIMULATED TRANSDUCER.

F_r	4.51 MHz
F_a	5.38 MHz
k_t	0.58
C_0	85.40 pF
$ Z(F_r) $	49.06 Ω
F_c	4.54 MHz
LCF(@ -6dB)	4.30 MHz
HCF(@ -6dB)	4.79 MHz
BW(@ -6dB)	10.90%
$U_n(F_c)$	2.05 nm/V
$\Pi(F_c)$	7.34 mW/V

Parameters: F_r is the resonance frequency, F_a is the antiresonance frequency, k_t is the thickness mode coupling factor, C_0 is the static capacitance, $|Z(F_r)|$ is the electrical impedance module at the resonance frequency, F_c is the central frequency for which the radiated power is maximum, LCF(@ -6dB) is the low cutoff frequency at -6 dB of the radiated power, HCF(@ -6dB) is the high cutoff frequency at -6 dB of the radiated power, BW(@ -6dB) is the bandwidth at -6 dB of the radiated power, $U_n(F_c)$ is the average normal displacement over the radiating surface of the transducer at the central frequency, and $\Pi(F_c)$ is the radiated acoustic power at the central frequency.

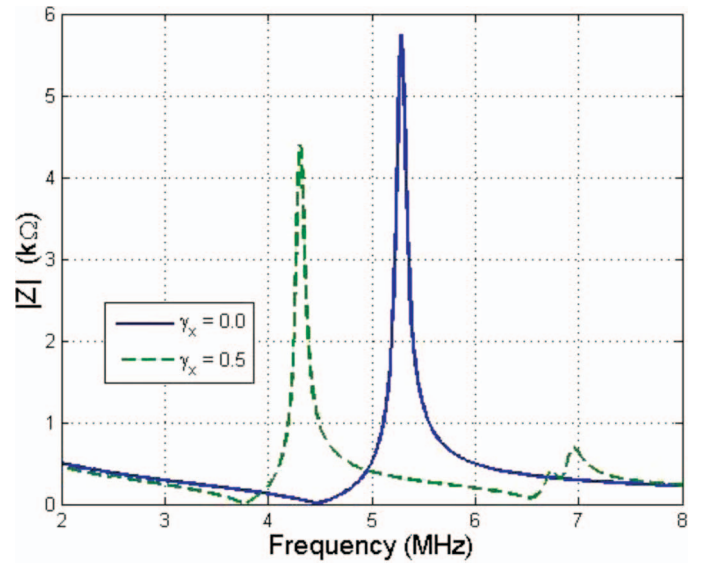


Fig. 7. Electrical harmonic impedance of the transducer in vacuum versus frequency for two values of the Floquet parameter γ_x .

knowledge of the geometrical shape of the heterogeneity. As one can see on this figure, the acoustic intensity is well focused on the elliptic path surrounding the tumor. One can also observe significant acoustic intensities for some regions outside of the desired path. This is due to the adaptive focusing strategy that enhanced the superposition of US beams in regions near the linear arrays forming the octagonal probe. For practical implementation, no *a priori* on the lesion geometry may be necessary if one sequentially and automatically targets different closed ROIs within the breast.

Fig. 9(b) shows the calculated stationary displacement field in the ROI at the central frequency of propagating shear waves, which was calculated by considering the mean acoustic radiation forces of Fig. 9(a) coupled to the FEM simulations. More specifically, the displacement field is the magnitude of displacements calculated from the Cartesian

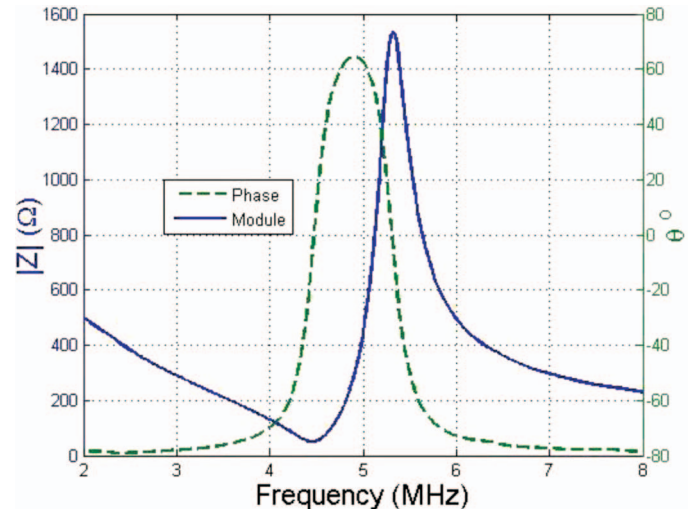


Fig. 8. Electrical impedance of the transducer in water versus frequency (θ is the phase angle).

TABLE V. SIMULATED RANGES OF ELECTRICAL EXCITATION PARAMETERS OF THE OCTAGONAL ARRAY TRANSDUCER.

$ \Phi_0 $	0.45 to 0.92 V
Maximum of $ \Phi_i $	1.06 to 1.60 V
Number of firing elements $N_{ap} + 1$ per focal point	95 to 215

components of the displacement vectors. Physically, this is the magnitude of the torsional displacement induced by the combination of the radiation forces. According to this figure, it is clearly observable that generated shear waves follow well the imposed generation path. Indeed, shear waves have an elliptical shape and exhibit a focusing effect near and into the mechanical heterogeneity. This results in an increase of the displacement intensity into the simulated tumor.

To conclude, this example shows the potential of 2-D radiation forces in the context of breast tumor elastography. By soundly concentrating the shear wave energy, the gain in displacement amplitude should permit enhancement of the elastographic image quality and contribute to perform precise viscoelastic characterization and mapping. To ensure an optimal shear wave convergence, the proposed approach permits generation of convergent shear waves following adaptive paths by properly considering the tumor shape and position.

IV. DISCUSSION

The manual palpation of breasts to detect hard nodules is the primary screening method of cancer. Although a lesion may be missed on mammograms or incorrectly identified as benign or malignant with B-mode US and/or magnetic resonance imaging, it usually involves changes in mechanical properties resulting from cellular modifications and neovascularization. In this study, we proposed the theoretical design of an octagonal probe for generating radiation pressure sources around a suspected lesion and in-going propagating shear waves. By experimentally tracking these waves to map the displacement field and by formulating an appropriate inverse problem, quantitative viscoelasticity assessments of breast lesions may be feasible. Our long-term vision is to develop a noninvasive scanning instrument based on the octagonal probe design to produce 2-D or 3-D breast reconstructions of its viscoelasticity for screening and diagnosis. This could be implemented in the framework of our recently developed shear-wave-induced resonance elastography (SWIRE) method [20]. Three-dimensional images would be obtained by translating the probe of Fig. 3 from the thorax to the extremity of the breast. With the current design, another superimposed array would be necessary for optimal imaging of propagating shear waves because the octagonal probe was designed to optimize the transmission of acoustic power at a low excitation voltage (to optimize the connectivity with standard US scanner because of the possibility of generating radiation pressures without specific

changes of the front-end of the scanner or adaptation of the power supply).

In the current study, 1–3 piezocomposite material was optimized and used to design a high-sensitivity transducer with two layers without backing. The transducer elements

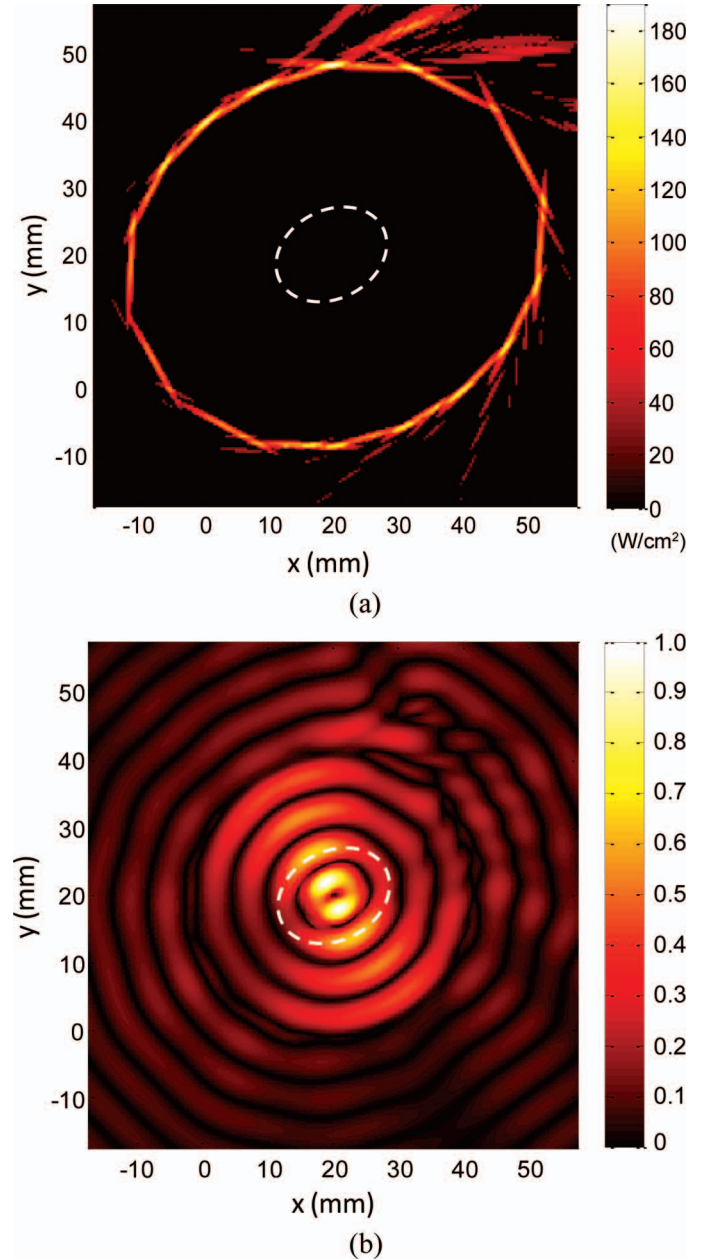


Fig. 9. (a) Acoustic intensity in watts per centimeter squared induced by successively focused ultrasound beams around the idealized elliptic tumor (represented by a dashed line). (b) The corresponding simulated normalized $[0,1]$ displacement field induced by the adaptive radiation force. Shear displacement is more important into the elliptic heterogeneity because of the wave focusing effect. 

were optimized for a central frequency of 4.54 MHz. To adapt the shear wave front to the tumor location and geometry, a focusing strategy presented in Section III-C was developed and theoretically implemented. Acoustic simulations were performed with an exact linear formulation. The low-amplitude electrical excitation that could generate the radiation force along a path and the resulting acoustic pattern in a ROI were evaluated. The magnitude and orientation of the acoustic intensity (radiation force) could be controlled at any point along a path that was circular for the example presented in this study. Because of the low-voltage excitation level, we predict that transducer overheating would be negligible. US beam forming simulations were then coupled to low-frequency elastodynamic simulations. In-going shear waves matching the tumor contour could be obtained and shear wave displacements in the tumor were increased with respect to surrounding tissues outside the ROI. The proposed transducer design theoretically allowed enhancing of the tissue mechanical response by respecting the safety limitations on the acoustic power deposited by US focusing. The next step would be to fabricate the phased array with its control electronics for experimental evaluations.

As introduced earlier, a possible improvement of this work would be the design of a dual US phased array that would generate a radiation force and perform imaging of propagating shear waves. To achieve these specifications, the transducer bandwidth would have to be above 60% if RF shear wave tracking is envisaged or lower for Doppler-based tracking methods. Whatever the tracking strategy adopted, B-mode imaging would be an important option and a large bandwidth would thus be required. The US transducer bandwidth is mainly limited by the first lateral mode. To overcome this problem, one solution would be to use a ceramic phase with a high shear velocity. However, the coupling factor, the dielectric constant, and the mechanical impedance would likely not be in acceptable ranges. Another solution would be to design pseudo-random 1–3 piezocomposite transducer textures.

V. CONCLUSION

All major organizations recommend X-ray mammography with screening programs varying from annual evaluation beginning at 40 years of age to biannual mammography for women older than 50. Mammography reduces breast cancer mortality by 20% to 35% for women between 50 and 69 years of age, and slightly less in younger women [32]. In the sub-population of young pre-menopausal women, the sensitivity of mammography is decreased because of the high breast parenchyma density that reduces image contrast. Consequently, X-ray mammography can detect approximately 85% of cancer tumors in women aged over 50, but only 50% to 70% of malignant lesions in younger women with dense breast parenchyma [32], [33]. On the other hand, many women are re-called after screening mammography for investigation of abnormali-

ties which are subsequently found not to be malignant. Indeed, approximately 95% of suspected abnormalities on mammograms are not cancerous (poor specificity) [32]. The exact nature of the lesion is verified by additional mammographic views or standard US, with occasional use of magnetic resonance imaging for select cases. When suspicious enough, percutaneous biopsy or surgical excision confirms the diagnosis, where histopathology is used for therapy planning. Compared with existing dynamic US elastography methods, our technique may be advantageous because of its high flexibility to generate different shear wave fronts and its possible integration into a dedicated 3-D US dynamic elastography scanner for screening and diagnosis.

ACKNOWLEDGMENTS

The authors wish to thank Dr. M. Lukacs from Dr. F. S. Foster's Laboratory at the Sunnybrook Health Sciences Centre, Toronto, ON, Canada, for helpful discussions, and Dr. I. Trop from the University of Montreal Hospital for providing the clinical image for Fig. 4.

REFERENCES

- [1] J. Ophir, E. I. Céspedes, H. Ponnekanti, Y. Yazdi, and X. Li, "Elastography: A quantitative method for imaging the elasticity in biological tissues," *Ultrason. Imaging*, vol. 13, no. 2, pp. 111–134, 1991.
- [2] A. Itoh, E. Ueno, E. Tohno, H. Kamma, H. Takahashi, T. Shiina, M. Yamakawa, and T. Matsumura, "Breast disease: Clinical application of US elastography for diagnosis," *Radiology*, vol. 239, no. 2, pp. 341–350, 2006.
- [3] A. Thomas, S. Kümmel, F. Fritzsche, M. Warm, B. Ebert, B. Hamm, and T. Fischer, "Real-time sonoelastography performed in addition to B-mode ultrasound and mammography: Improved differentiation of breast lesions?" *Acad. Radiol.*, vol. 13, no. 12, pp. 1496–1504, 2006.
- [4] E. S. Burnside, T. J. Hall, A. M. Sommer, G. K. Hesley, G. A. Sissney, W. E. Svensson, J. P. Fine, J. Jiang, and N. J. Hangiandreou, "Differentiating benign from malignant solid breast masses with US strain imaging," *Radiology*, vol. 245, no. 2, pp. 401–410, 2007.
- [5] F. K. H. I. Schaefer, P. J. Schaefer, C. Mundhenke, S. Osterholz, B. M. Order, N. Hofheinz, J. Hedderich, M. Heller, W. Jonat, and I. Schreer, "Breast ultrasound elastography—Results of 193 breast lesions in a prospective study with histopathologic correlation," *Eur. J. Radiol.*, vol. 77, no. 3, pp. 450–456, 2011.
- [6] J. H. Yoon, M. H. Kim, E. K. Kim, H. J. Moon, J. Y. Kwak, and M. J. Kim, "Interobserver variability of ultrasound elastography: How it affects the diagnosis of breast lesions," *AJR Am. J. Roentgenol.*, vol. 196, no. 3, pp. 730–736, 2011.
- [7] A. Thitaikumar, L. M. Mobbs, C. M. Kraemer-Chant, B. S. Garra, and J. Ophir, "Breast tumor classification using axial shear strain elastography: A feasibility study," *Phys. Med. Biol.*, vol. 53, no. 17, pp. 4809–4823, 2008.
- [8] R. M. Lerner, S. R. Huang, and K. J. Parker, "'Sonoelasticity' images derived from ultrasound signals in mechanically vibrated tissues," *Ultrasound Med. Biol.*, vol. 16, no. 3, pp. 231–239, 1990.
- [9] Y. Yamakoshi, J. Sato, and T. Sato, "Ultrasonic imaging of internal vibration of soft tissue under forced vibration," *IEEE Trans. Ultrason. Ferroelectr. Freq. Control*, vol. 37, no. 2, pp. 45–53, 1990.
- [10] A. P. Sarvazyan, O. V. Rudenko, S. D. Swanson, J. B. Fowlkes, and S. Y. Emelianov, "Shear wave elasticity imaging—A new ultrasonic technology of medical diagnostic," *Ultrasound Med. Biol.*, vol. 20, no. 9, pp. 1419–1436, 1998.
- [11] J. Bercoff, S. Chaffai, M. Tanter, L. Sandrin, S. Catheline, M. Fink, J. L. Gennisson, and M. Meunier, "In vivo breast tumor detection

- using transient elastography," *Ultrasound Med. Biol.*, vol. 29, no. 10, pp. 1387–1396, 2003.
- [12] A. Athanasiou, A. Tardivon, M. Tanter, B. Sigal-Zafrani, J. Bercoff, T. Defieux, J. L. Gennisson, M. Fink, and S. Neuenchwander, "Breast lesions: Quantitative elastography with supersonic shear imaging—Preliminary results," *Radiology*, vol. 256, no. 1, pp. 297–303, 2010.
- [13] A. Evans, P. Whelehan, K. Thomson, D. McLean, K. Brauer, C. Purdie, L. Jordan, L. Baker, and A. Thompson, "Quantitative shear wave ultrasound elastography: Initial experience in solid breast masses," *Breast Cancer Res.*, vol. 12, no. 6, pp. R104–R114, 2011.
- [14] W. A. Berg, D. O. Cosgrove, C. J. Doré, F. K. W. Schäfer, W. E. Svensson, R. J. Hooley, R. Ohlinger, E. B. Mendelson, C. Balu-Maestro, M. Locatelli, C. Tourasse, B. C. Cavanaugh, V. Juhán, A. T. Stavros, A. Tardivon, J. Gay, J. P. Henry, and C. Cohen-Bacrie, "Shear-wave elastography improves the specificity of breast US: The BE1 multinational study of 939 masses," *Radiology*, vol. 262, no. 2, pp. 435–449, 2012.
- [15] J. Bercoff, M. Tanter, and M. Fink, "Supersonic shear imaging: A new technique for soft tissue elasticity mapping," *IEEE Trans. Ultrason. Ferroelectr. Freq. Control*, vol. 51, no. 4, pp. 396–409, 2004.
- [16] C. Hazard, Z. Hah, D. Rubens, and K. Parker, "Integration of crawling waves in an ultrasound imaging system. Part 1: System and design considerations," *Ultrasound Med. Biol.*, vol. 38, no. 2, pp. 296–311, 2012.
- [17] M. Fatemi and J. F. Greenleaf, "Vibro-acoustography: An imaging modality based on ultrasound-stimulated acoustic emission," *Proc. Natl. Acad. Sci. USA*, vol. 96, no. 12, pp. 6603–6608, 1999.
- [18] K. R. Nightingale, M. L. Palmeri, R. W. Nightingale, and G. E. Trahey, "On the feasibility of remote palpation using acoustic radiation force," *J. Acoust. Soc. Am.*, vol. 110, no. 1, pp. 625–634, 2001.
- [19] A. Hadj Henni, C. Schmitt, and G. Cloutier, "Shear wave induced resonance elastography of soft heterogeneous media," *J. Biomech.*, vol. 43, no. 8, pp. 1488–1493, 2010.
- [20] A. Hadj Henni, C. Schmitt, I. Trop, and G. Cloutier, "Shear wave induced resonance elastography of spherical masses with polarized torsional waves," *Appl. Phys. Lett.*, vol. 100, no. 13, art. no. 133702, 2012.
- [21] E. E. Konofagou and K. Hynynen, "Localized harmonic motion imaging: theory, simulations and experiments," *Ultrasound Med. Biol.*, vol. 29, no. 10, pp. 1405–1413, 2003.
- [22] S. McAleavey, M. Menon, and E. Elegbe, "Shear modulus imaging with spatially-modulated ultrasound radiation force," *Ultrason. Imaging*, vol. 31, no. 4, pp. 217–234, 2009.
- [23] S. Chen, M. W. Urban, C. Pislaru, R. Kinninck, Y. Zheng, A. Yao, and J. F. Greenleaf, "Shearwave dispersion ultrasound vibrometry (SDUV) for measuring tissue elasticity and viscosity," *IEEE Trans. Ultrason. Ferroelectr. Freq. Control*, vol. 56, no. 1, pp. 55–62, 2009.
- [24] M. P. André, H. S. Janée, P. J. Martin, G. P. Otto, B. A. Spivey, and D. A. Palmer, "High-speed data acquisition in a diffraction tomography system employing large-scale toroidal arrays," *Int. J. Imaging Syst. Technol.*, vol. 8, no. 1, pp. 137–147, 1997.
- [25] R. C. Waag and R. J. Fedewa, "A ring transducer system for medical ultrasound research," *IEEE Trans. Ultrason. Ferroelectr. Freq. Control*, vol. 53, no. 10, pp. 1707–1718, 2006.
- [26] J. Rouyer, S. Mensah, E. Franceschini, P. Lasaygues, and J. P. Lefebvre, "Conformal ultrasound imaging system for anatomical breast inspection," *IEEE Trans. Ultrason. Ferroelectr. Freq. Control*, vol. 59, no. 7, pp. 1457–1469, 2012.
- [27] G. Harris and R. Phillips, "Guidance for Industry and FDA Staff: Information for Manufacturers Seeking Marketing Clearance of Diagnostic Ultrasound Systems and Transducers," U.S. Department of Health and Human Services, Food and Drug Administration, Center for Devices and Radiological Health, Silver Spring, MD, 2008.
- [28] D. Berlincourt and H. H. A. Krueger, "Properties of piezoelectricity ceramics mapping," MTC ElectroCeramics, Thornhill, UK, Technical publication TP-226, 2011, pp. 1–12.
- [29] W. A. Smith and B. A. Auld, "Modeling 1-3 composite piezoelectrics: Thickness-mode oscillations," *IEEE Trans. Ultrason. Ferroelectr. Freq. Control*, vol. 38, no. 1, pp. 40–47, 1991.
- [30] J. M. Cannata, T. A. Ritter, W. H. Chen, R. H. Silverman, and K. K. Shung, "Design of efficient, broadband single-element (20–80 MHz) ultrasonic transducers for medical imaging applications," *IEEE Trans. Ultrason. Ferroelectr. Freq. Control*, vol. 50, no. 11, pp. 1548–1557, 2003.
- [31] M. Draheim and W. Cao, "Finite element analysis impedance matching layer thickness," in *IEEE Ultrasonics Symposium*, 1996, pp. 1015–1017.
- [32] J. G. Elmore, K. Armstrong, C. D. Lehman, and S. W. Fletcher, "Screening for breast cancer," *JAMA*, vol. 293, no. 10, pp. 1245–1256, 2005.
- [33] T. M. Kolb, J. Lichy, and J. H. Newhouse, "Comparison of the performance of screening mammography, physical examination, and breast US and evaluation of factors that influence them: An analysis of 27,825 patient evaluations," *Radiology*, vol. 225, no. 1, pp. 165–175, 2002.



Didace Ekeom received D.E.A. (diplôme d'Etude Approfondie) and Ph.D. degrees in mechanics from IEMN-CNRS, Université des Sciences et Techniques de Lille, France. He has been working on FEM-BEM modeling of transducer radiation in oil boreholes. In 1998, he joined the CEMEF-CNRS, École des Mines de Paris, France, where he worked on inverse numerical modeling for rheological parameter identification. In 2001, he joined the LUSSI, Université François Rabelais de Tours, France, where he worked on CMUT transducer modeling and characterization. In 2004, he joined Microsonics, where his work focuses on FEM-BEM modeling of BAW and MEMS resonators. While maintaining his affiliation with Microsonics, he worked between 2009 and 2010 as a scientist in the Laboratory of Biorheology and Medical Ultrasonics of the University of Montreal Hospital Research Center.



Anis Hadj Henni was born in 1979 in Algiers, Algeria. He received his engineering degree in civil engineering from the National Polytechnic School of Algiers in 2002. In 2006, he received his Ph.D. degree in mechanics from the Université de Bordeaux I, France, for his work on microwave generation of vibrations applied to nondestructive evaluation of structures. In 2006, he joined, as a postdoctoral fellow, the Laboratory of Biorheology and Medical Ultrasonics (LBUM, CRCHUM) in Montreal to work on dynamic elastography imaging of soft tissues. He then obtained a position of Research Associate in this laboratory. Currently, Dr. Hadj Henni holds the position of President of Rheolution Inc., Montreal, Canada, where he develops innovative spectroscopic mechanical instruments for industrial and biomedical applications.



Guy Cloutier (S'89–M'90–SM'07) obtained his B.Eng. degree in electrical engineering in 1984, and M.Sc. and Ph.D. degrees in biomedical engineering in 1986 and 1990, respectively. Between 1990 and 1992, he was a postdoctoral fellow at The Pennsylvania State University with Prof. K. Kirk Shung. Prof. Cloutier is Director of the Laboratory of Biorheology and Medical Ultrasonics at the University of Montreal Hospital Research Center (www.lbum-crchum.com), and Professor of Radiology and Biomedical Engineering at the University of Montreal. His research interests are in quantitative ultrasound imaging of red blood cell aggregation; quasi-static and dynamic ultrasound elastography of atherosclerotic plaques, vascular aneurysms, deep vein thrombi, and breast cancers; 3-D morphologic and hemodynamic assessment of lower-limb arterial stenoses; and mathematical and biomechanical modeling. He has published more than 135 peer-reviewed articles in these fields, holds 8 patents, and was recipient of the National Scientist award of the Fonds de la Recherche en Santé du Québec (2004–2009).